

1. Role of lattice parameters on heterogeneous ice nucleation

Ice nucleating agents such as silver iodide (AgI), used for cloud seeding induce ice formation at relatively high temperatures between 0 and -5 °C [Pruppacher and Klett, 1978; Bruintjes, 1999]. It has been often assumed that the good ice nucleation ability of AgI is due to the small lattice mismatch between its surface and the hexagonal ice [Vonnegut, 1947; Pruppacher and Klett, 1978]. However, recent molecular dynamics simulation indicate that a good lattice match between both the surfaces is insufficient to predict the ice nucleation ability of AgI [Zielke et al., 2015]. The role that lattice matching plays in heterogeneous ice nucleation remains a debated issue. Moreover, many authors have concluded that the lattice matching can serve as a good condition, but not a requirement/guaranty for the onset of ice nucleation [Sadtschenko et al., 2002; Nutt and Stone, 2002, 2004; Hu and Michaelides, 2007; Cox et al., 2012; Reinhardt and Doye, 2014; Fitzner et al., 2015; Marcolli et al., 2016].

The following tables (Table 1 and 2) show the crystallographic data of the pyroelectric single crystals and the hexagonal ice I_h .

Table 1: Crystallographic properties of the pyroelectric single crystals and of hexagonal ice I_h at $T = 250$ K.

	LiNbO₃ (LN) ^a	LiTaO₃ (LT) ^b	Sr_xBa_{1-x}Nb₂O₆ (SBN) ^{c,*}	ice I_h ^d
point group	3m (C _{3v})	3m (C _{3v})	4mm (C _{4v})	6/mmm (D _{6h})
space group	R3c	R3c	P4bm	P6 ₃ /mmc
a (Å)	5.148	5.154	12.481 / 12.430	4.5181
b (Å)	= a	= a	= a	= a
c (Å)	13.863	13.784	3.954 / 3.913	7.3560

^a [Abrahams et al., 1966]

^b [Abrahams and Bernstein, 1967]

^c [Jamieson et al., 1968; Megumi et al., 1976; Podlozhenov et al., 2006]

^d [La Placa and Post, 1960; Röttger et al., 1994]

^(*) $x = 0.5 / 0.75$, SBN(0.61) is congruent melting composition ($a=12.458$ Å, $c=3.938$ Å).

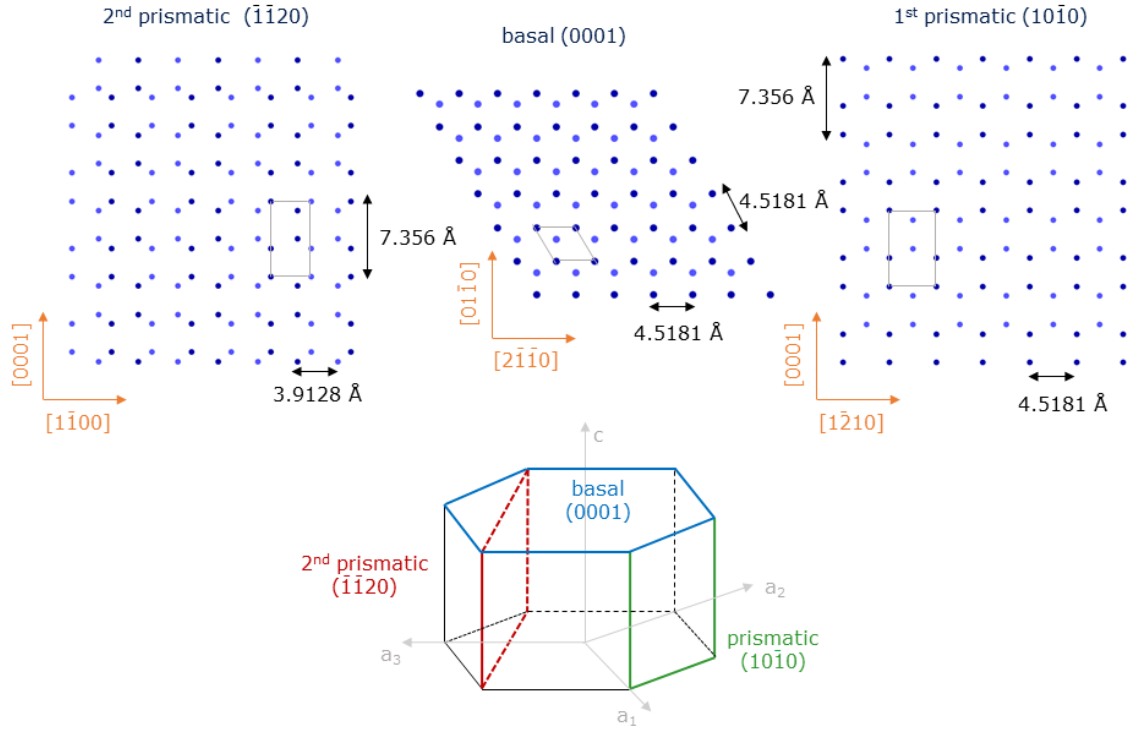


Figure 1: Illustration of the hexagonal ice I_h with its three crystal faces with their corresponding surface unit cells (gray rectangle or parallelogram).

Table 2: Lattice parameters of the surface unit cell of the three faces of hexagonal ice I_h .

	basal (0001)	1. prismatic (10 $\bar{1}$ 0)	2. prismatic (11 $\bar{2}$ 0)
surface unit cell	parallelogram	rectangle	rectangle
a (Å)	4.5181	4.5181	3.9128
b (Å)	= a	7.3560	3.7560

The lattice mismatch between the crystal face of hexagonal ice I_h , see Figure 1, and the polar surface of the pyroelectric single crystal can be calculated using the lattice parameters of both crystals:

$$\delta = \frac{a_{\text{substrate}} - a_{\text{ice}}}{a_{\text{ice}}}$$

The orthogonal (x, y, z) coordinate system was used for the calculation of the lattice mismatch, with the x -axis and the z -axis parallel to the a_1 -axis and the c -axis of the hexagonal (a_1, a_2, a_3, c) coordinate system, respectively. The polar surface of the pyroelectric single crystal used the orthogonal coordinate system and one of three crystal face of ice I_h with its corresponding coordinate system (either orthogonal or hexagonal) was compared to it. In the case of SBN there are two relevant possibilities to arrange the coordinate system of the ice crystal: parallel or 45° rotated relative to the x - and y -axis of the crystal coordinate system. Then the lattice mismatch was calculated in two directions (x - and y -axis of the crystal face of ice I_h).

Due to the parameter similarity between LN and LT the mismatch difference between both single crystals and hexagonal ice is expected to be negligibly small (see Table 3).

Table 3: Lattice mismatch between the crystal face of hexagonal ice I_h (column) and the polar surface site of the pyroelectric single crystal (row).

		basal (0001)	1. prismatic (10$\bar{1}$0)	2. prismatic (11$\bar{2}$0)
LN	x -axis	13.94 %	13.94 %	31.57 %
	y -axis	13.94 %	21.22 %	21.22 %
LT	x -axis	14.07 %	14.07 %	31.72 %
	y -axis	14.07 %	21.36 %	21.36 %
SBN	x -axis	(38.12 / 37.56) %	(38.12 / 37.56) %	(59.49 / 58.84) %
	y -axis	(-20.26 / -20.58) %	(-15.16 / -15.51) %	(-15.16 / -15.51) %
	45°	(-2.33 / -2.73) %	(-2.33 / -2.73) %	(12.78 / 12.32) %
		(12.78 / 12.32) %	(19.98 / 19.49) %	(19.98 / 19.49) %

The lattice mismatch between SBN single crystal and three ice faces is in most cases significantly larger than that of both LN and LT. An exception occurs when the ice crystal face is rotated at an angle of 45° along the z -axis of the pyroelectric single crystal system. On the basis of these results it can be possibly expected that heterogeneous ice nucleation is enhanced on LN and LT single crystal surfaces compared to SBN. This would explain the lower icing temperature on both oppositely charged SBN surfaces in comparison with that on both surfaces of LN (see Figures 3-5). The substantial icing temperature difference between LN and LT despite their similar lattice parameters indicates that the surface structure geometry does not play an

important role on heterogeneous ice nucleation in relation to the water freezing induced by the pyroelectric effect.

2. Surface roughness of the inner wall of the three ring systems

In order to analyze the surface roughness of the inner wall of the ring system, scanning electron microscopy (SEM) images were made on each of them (Figures 2-4). These three ring systems were processed by different means in several institutes: the aluminum ring was mechanically drilled and polished, the steel ring was laser cut and then mechanically polished, and the plastic ring was milled. By comparing the SEM images, it can be observed that the aluminum ring possesses the most uniform and smoothest surface. On the other hand, the inner wall of the steel ring shows noticeable traces/tracks of laser cutting, the so-called melt zone. Surprisingly, many ridges are clearly recognizable over inner wall of the plastic ring. The grooves on the inner walls of all ring systems are the result of surface polishing or milling. Their height was determined to be less than $1.5\ \mu\text{m}$ for aluminum and steel rings (Figure 5 (a)-(d)). The ridges distributed over the inner wall of the plastic ring show different heights ranging from a few μm to $50\ \mu\text{m}$ (Figure 5 (e)). The relatively smooth surface of the aluminum ring is suggested to be the appropriate choice for the reduction of the roughness effect on heterogeneous ice nucleation, as the comparison in Figure 7 of the paper indicates the lowest icing temperature of water was observed for the aluminum ring, when compared to both other ring materials.

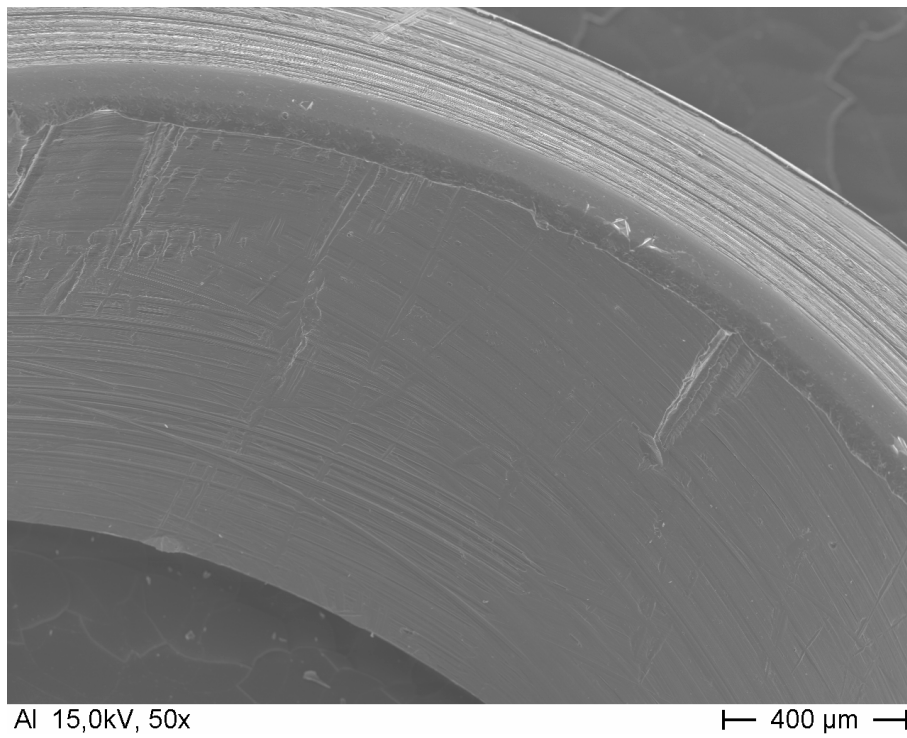


Figure 2: SEM images of the inner wall of the aluminum ring, (b) steel ring, and (c) polyamide plastic ring imaged using a 45° tilted sample holder.

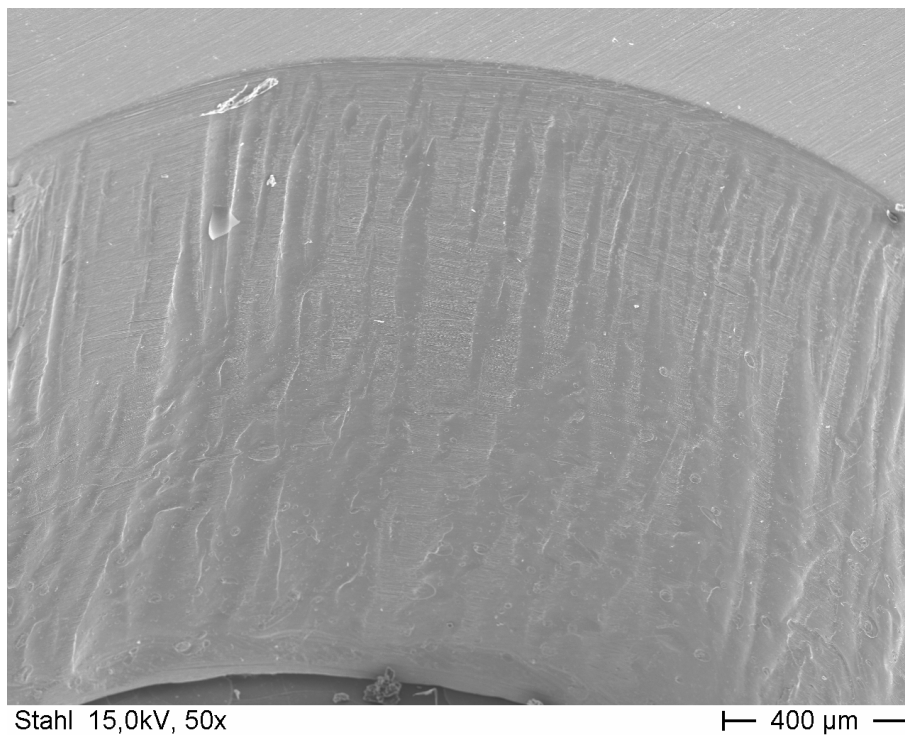


Figure 3: SEM images of the inner wall of the steel ring imaged using a 45° tilted sample holder.

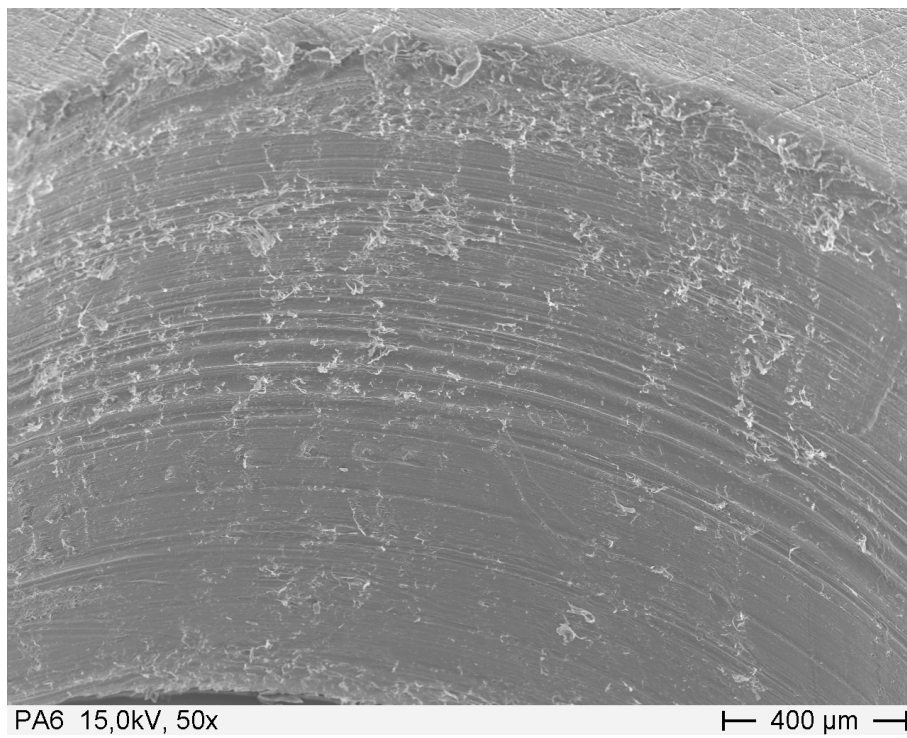


Figure 4: SEM images of the inner wall of the polyamide plastic ring imaged using a 45° tilted sample holder.

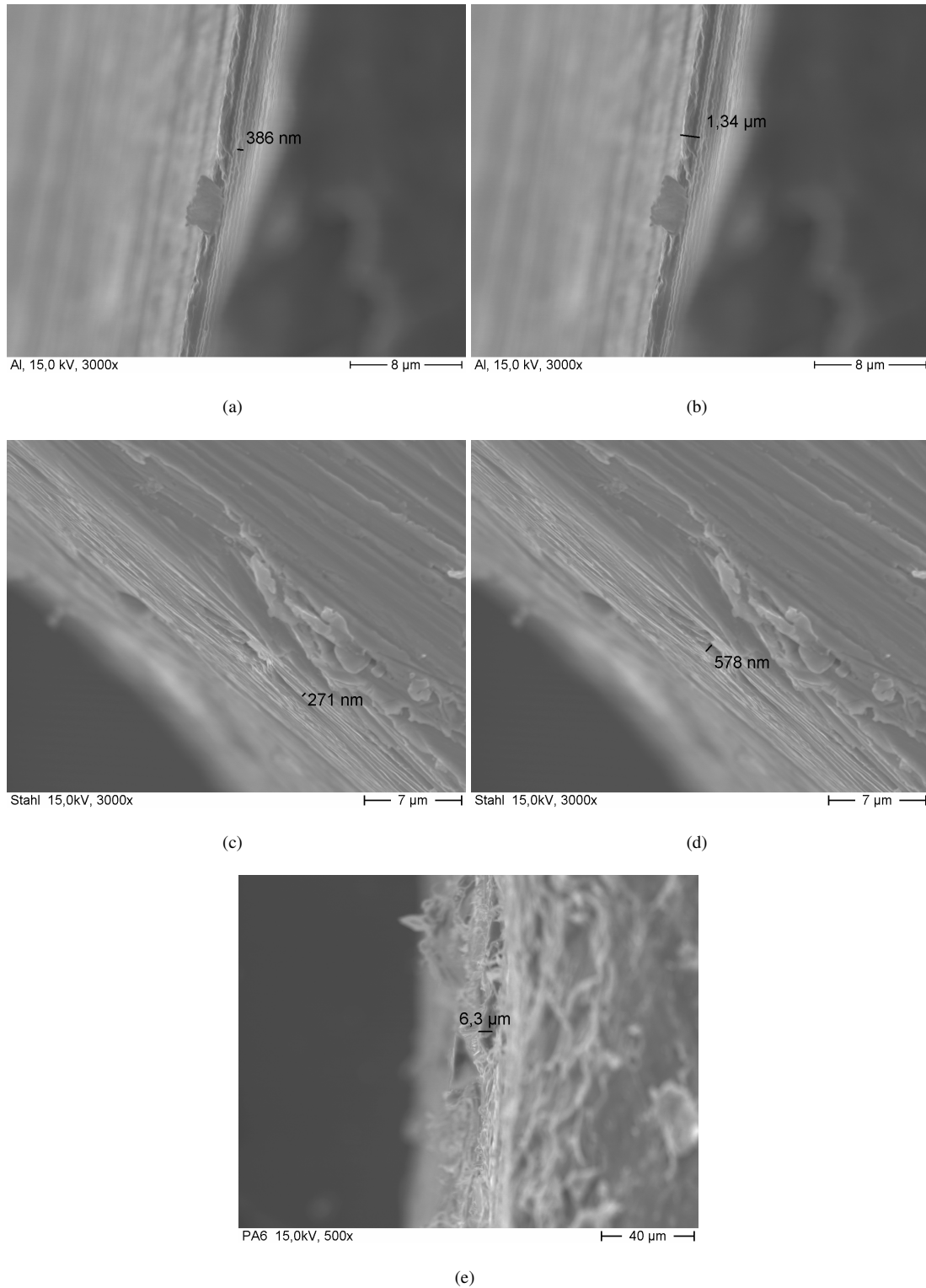


Figure 5: SEM images with the height indication of the grooves on the inner wall of the (a),(b) aluminum ring and (c),(d) steel ring, and of the ridges on the inner wall of the (e) the polyamide plastic ring. All images use a perspective parallel to the inner wall surface.

3. Contact angle hysteresis of the sessile water droplet on different pyroelectric single crystals

In order to determine the wetting properties (hydrophobicity/hydrophilicity) of pyroelectric single crystals a dynamic contact angle measurement was performed on each one. The adsorption of water onto a solid surface is defined by the balance between the adhesive and cohesive forces of water. The adhesive force is a measure for the hydrogen bonding strength between the water molecules and the substrate. As it is increased relative to the cohesive force, there is an increase in the water contact area with the substrate and therefore also a reduction in the contact angle. This is the case of hydrophilic surfaces having hydrogen bonding sites with strong bonding strength. The contact angle hysteresis, defined as the difference between the advancing and receding contact angle of a liquid droplet on a solid surface, is influenced by physical and chemical surface heterogeneities. These can affect the thermodynamic behavior of water molecules at the solid-liquid interface during the supercooling of water [Heydari et al., 2013].

The OCA 15EC (Dataphysics) in combination with the temperature and humidity control chamber (TPC 160 combined with the humidity generator HGC 20, Dataphysics) was used for the dynamic contact angle measurements and droplet shape analysis (Figure 6). A syringe with distilled water was positioned directly above the pyroelectric single crystal sample so that the drained water droplet can be in direct contact with both the substrate and the needle. A direct contact with the needle is necessary in order to increase and decrease the water droplet volume for the determination of the advancing and receding contact angles, respectively. Prior to the measurement, a very small water droplet of about $0.5 \mu\text{l}$ was deposited on the single crystal surface in order to prevent the any unwanted side-slipping of drained water from the needle. Then two drainage cycles of $10 \mu\text{l}$ water were run with increasing and decreasing volume rates of $1 \mu\text{l}/\text{min}$. A hold time of 2 s was set between the water volume changes. An air humidity of about 30 % at room temperature was set as an initial value before the start of the experimental cycles. At least 4 tests were made on each sample type and surface. Five conditions were chosen for the analysis of the temperature dependence of the water contact angle and the influence of pyroelectricity on water wetting behavior: Firstly the contact angle was determined at room temperature (21°C), then the sample was cooled at the rate of $1^\circ\text{C}/\text{min}$ to the new constant temperature of 10°C and during cooling the contact angle was measured. After making measurements at this fixed temperature, the sample was cooled again at the same rate to the temperature of 5°C , again contact angle measurements were made during cooling and at 5°C .

The advancing contact angle of the sessile water droplet remain nearly unchanged in all conditions, with the exception of a slightly lower contact angle values on the positively charged LN surface (LN(+)) in Figure 7 (a)). Only after decreasing the water volume (receding contact angle), the differences between different samples and their surfaces become clearer. All samples show a different contact angle hysteresis

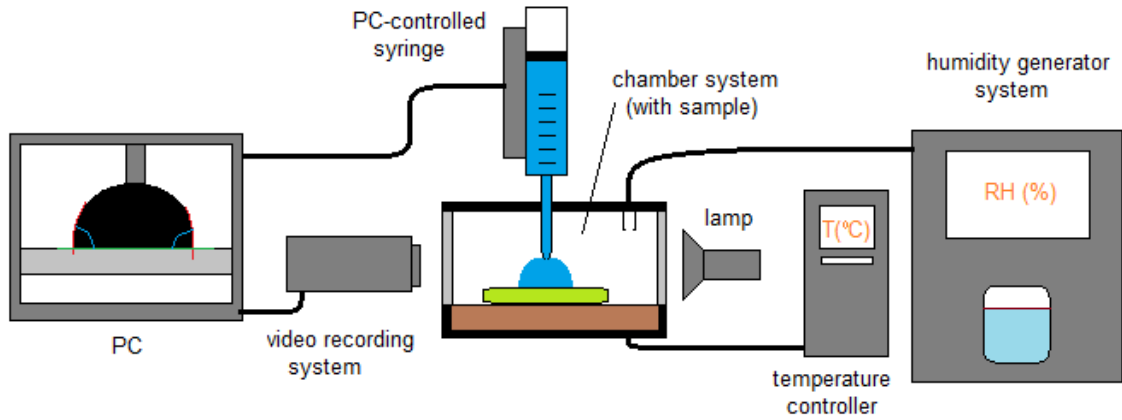


Figure 6: Sketch of the measurement setup.

on both surfaces (Figure 7 (b) and (c)). Both oppositely charged surfaces of SBN and LT have contrasting tendencies, where either the contact angle increases or decreases during the cooling. In the first step the negatively charged surfaces become more hydrophilic in relation to the positively charged during cooling from 21 to 10 °C, then the water adhesion on negatively charged surface decreases in the second cooling period between 10 and 5 °C, becoming more hydrophobic in relation to the positively charged surface at 5 °C. Contrastingly, the LN shows the contra water adhesion behavior on both charged surfaces. Remarkably, the contact angle difference of about 10 ° between oppositely charged surfaces of a pyroelectric single crystal increases at the end of a cycle (Figure 7 (c)). This may explain the small icing temperature differences of sessile water droplet on SBN and LT, since the higher surface hydrophobicity may compensate the pyroelectrically induced freezing delay. For comparison, the lower surface hydrophobicity of negatively charged surface of LN enables stronger wetting, which due to the associated higher contact area can be expected to enhance the pyroelectric effect on the freezing delay (when measured with the sessile droplet method).

Therefore, neither a distinct correlation nor significant differences can be found between the contact angle hysteresis and the freezing nor the contact angle hysteresis and the pyroelectrically induced surface charge of the different single crystals, respectively.

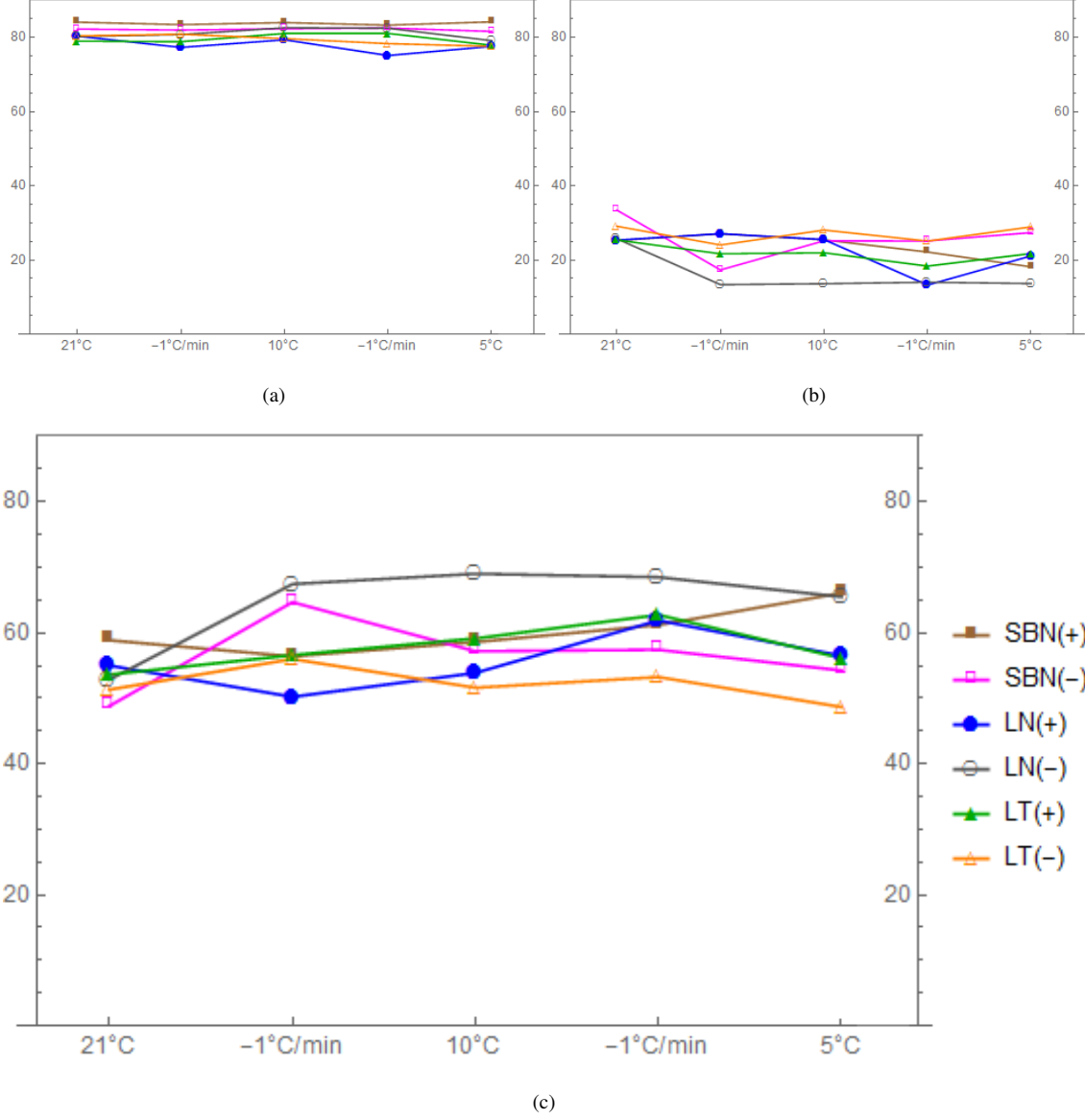


Figure 7: Temperature-dependent contact angles (CA) of sessile water droplet on both surfaces of three different pyroelectric single crystal samples: (a) advancing CA, (b) receding CA and (c) CA hysteresis. The horizontal axis is either the constant temperature or cooling period between the constant temperatures and the vertical axis the contact angle value.

4. Effect of cooling rate on water freezing

In all of the measurements the cooling rate of the silver heating stage was set to 1 °C/min. In general, the choice of this value is influenced by the time required to obtain the icing temperature data, although temperature changes in natural surroundings are usually lower. For industrial applications (refrigerator, ice box) or engineering systems (aircraft, wind turbine, weather station) the defined cooling rates within the thermal cycles are usually higher than 1 °C/min. Therefore, it has been assumed that a cooling rate of 1 °C/min is a reasonable compromise for most applications. The cooling rate exerts a measurable influence on the degree of water droplet supercooling. On the one hand, for high cooling rates the bulk temperature of water will lag further behind the stage temperature than for low rates due to different thermal capacities and conductivities of the stage material and the sample inclusive water. As a consequence, larger temperature gradients and thus stronger thermal convections are expected to arise inside the droplet, which in turn alter the ice crystallization behavior. On the other hand, a lower cooling rate of the stage material leads to a more uniform temperature profile in the sample system. However, while the water bulk temperature varies slowly with time, the time-dependent contribution of heterogeneous ice nucleation rate will be an important factor determining the freezing behavior during the supercooling. This is because of the nearly constant surface diffusivity of water molecules and molecular attachment/impingement rates in the vicinity of ice embryos randomly distributed over the sample surface under these conditions.

It is assumed that the cooling rate has an influence on the pyroelectric effect because the pyroelectrically induced surface charge is proportional to the rate of temperature change [Damjanovic, 1998]. Setting a higher cooling rate value leads to an enhanced pyroelectric effect due to the larger amount of surface charge and therefore a stronger associated electric field that can be expected to cause a stronger effect on the water molecule orientation near the solid surface. As a consequence, it would be reasonable to expect that a variation of the cooling rate can change the water freezing behavior and thus lead to different icing temperatures. For the goals of our experimental study interest was limited to the verification of the relationship between the pyroelectric coefficient and the water supercooling degree. On this basis the cooling rate was set at constant value for all experiments.

References

Abrahams, S., Bernstein, J., 1967. Ferroelectric lithium tantalate1. single crystal x-ray diffraction study at 24c. Journal of Physics and Chemistry of Solids 28, 1685 – 1692. URL: <http://www.sciencedirect.com/science/article/pii/0022369767901424>, doi:[https://doi.org/10.1016/0022-3697\(67\)90142-4](https://doi.org/10.1016/0022-3697(67)90142-4).

- Abrahams, S., Reddy, J., Bernstein, J., 1966. Ferroelectric lithium niobate. 3. single crystal x-ray diffraction study at 24c. *Journal of Physics and Chemistry of Solids* 27, 997 – 1012. URL: <http://www.sciencedirect.com/science/article/pii/0022369766900722>, doi:[https://doi.org/10.1016/0022-3697\(66\)90072-2](https://doi.org/10.1016/0022-3697(66)90072-2).
- Bruintjes, R.T., 1999. A review of cloud seeding experiments to enhance precipitation and some new prospects. *Bulletin of the American Meteorological Society* 80, 805–820. URL: [https://doi.org/10.1175/1520-0477\(1999\)080<0805:AROCSE>2.0.CO;2](https://doi.org/10.1175/1520-0477(1999)080<0805:AROCSE>2.0.CO;2), doi:10.1175/1520-0477(1999)080<0805:AROCSE>2.0.CO;2.
- Cox, S.J., Kathmann, S.M., Purton, J.A., Gillan, M.J., Michaelides, A., 2012. Non-hexagonal ice at hexagonal surfaces: the role of lattice mismatch. *Phys. Chem. Chem. Phys.* 14, 7944–7949. URL: <http://dx.doi.org/10.1039/C2CP23438F>, doi:10.1039/C2CP23438F.
- Damjanovic, D., 1998. Ferroelectric, dielectric and piezoelectric properties of ferroelectric thin films and ceramics. *Reports on Progress in Physics* 61, 1267. URL: <http://stacks.iop.org/0034-4885/61/i=9/a=002>.
- Fitzner, M., Sosso, G.C., Cox, S.J., Michaelides, A., 2015. The many faces of heterogeneous ice nucleation: Interplay between surface morphology and hydrophobicity. *Journal of the American Chemical Society* 137, 13658–13669. URL: <http://dx.doi.org/10.1021/jacs.5b08748>, doi:10.1021/jacs.5b08748.
- Heydari, G., Thormann, E., Jrn, M., Tyrode, E., Claesson, P.M., 2013. Hydrophobic surfaces: Topography effects on wetting by supercooled water and freezing delay. *The Journal of Physical Chemistry C* 117, 21752–21762. URL: <http://dx.doi.org/10.1021/jp404396m>, doi:10.1021/jp404396m.
- Hu, X.L., Michaelides, A., 2007. Ice formation on kaolinite: Lattice match or amphoterism? *Surface Science* 601, 5378 – 5381. URL: <http://www.sciencedirect.com/science/article/pii/S0039602807008692>, doi:<https://doi.org/10.1016/j.susc.2007.09.012>.
- Jamieson, P.B., Abrahams, S.C., Bernstein, J.L., 1968. Ferroelectric tungsten bronze-type crystal structures. i. barium strontium niobate $\text{Ba}_{0.27}\text{Sr}_{0.75}\text{Nb}_2\text{O}_{5.78}$. *The Journal of Chemical Physics* 48, 5048–5057. URL: <https://doi.org/10.1063/1.1668176>, doi:10.1063/1.1668176.
- La Placa, S.J., Post, B., 1960. Thermal expansion of ice. *Acta Crystallographica* 13, 503–505. URL: <http://dx.doi.org/10.1107/S0365110X60001205>, doi:10.1107/S0365110X60001205.

- Marcolli, C., Nagare, B., Welti, A., Lohmann, U., 2016. Ice nucleation efficiency of agi: review and new insights. *Atmospheric Chemistry and Physics* 16, 8915–8937. URL: <https://www.atmos-chem-phys.net/16/8915/2016/>, doi:10.5194/acp-16-8915-2016.
- Megumi, K., Nagatsuma, N., Kashiwada, Y., Furuhashi, Y., 1976. The congruent melting composition of strontium barium niobate. *Journal of Materials Science* 11, 1583–1592. URL: <https://doi.org/10.1007/BF00737513>, doi:10.1007/BF00737513.
- Nutt, D.R., Stone, A.J., 2002. Adsorption of water on the baf2(111) surface. *The Journal of Chemical Physics* 117, 800–807. URL: <https://doi.org/10.1063/1.1484377>, doi:10.1063/1.1484377.
- Nutt, D.R., Stone, A.J., 2004. Ice nucleation on a model hexagonal surface. *Langmuir* 20, 8715–8720. URL: <http://dx.doi.org/10.1021/la0489581>, doi:10.1021/la0489581.
- Podlozhenov, S., Graetsch, H.A., Schneider, J., Ulex, M., Wöhlecke, M., Betzler, K., 2006. Structure of strontium barium niobate $\text{Sr}_x\text{Ba}_{1-x}\text{Nb}_2\text{O}_6$ (sbn) in the composition range $0.32 \leq x \leq 0.82$. *Acta Crystallographica Section B* 62, 960–965. URL: <https://doi.org/10.1107/S0108768106038869>, doi:10.1107/S0108768106038869.
- Pruppacher, H.R., Klett, J.D., 1978. *Microphysics of Clouds and Precipitation*. Springer Netherlands. doi:10.1007/978-94-009-9905-3.
- Reinhardt, A., Doye, J.P.K., 2014. Effects of surface interactions on heterogeneous ice nucleation for a monatomic water model. *The Journal of Chemical Physics* 141, 084501. URL: <https://doi.org/10.1063/1.4892804>, doi:10.1063/1.4892804.
- Röttger, K., Endriss, A., Ihringer, J., Doyle, S., Kuhs, W.F., 1994. Lattice constants and thermal expansion of H_2O and D_2O ice Ih between 10 and 265 K. *Acta Crystallographica Section B* 50, 644–648. URL: <https://doi.org/10.1107/S0108768194004933>, doi:10.1107/S0108768194004933.
- Sadtchenko, V., Ewing, G.E., Nutt, D.R., Stone, A.J., 2002. Instability of ice films. *Langmuir* 18, 4632–4636. URL: <http://dx.doi.org/10.1021/la0255370>, doi:10.1021/la0255370.
- Vonnegut, B., 1947. The nucleation of ice formation by silver iodide. *Journal of Applied Physics* 18, 593–595. URL: <https://doi.org/10.1063/1.1697813>, doi:10.1063/1.1697813.
- Zielke, S.A., Bertram, A.K., Patey, G.N., 2015. A molecular mechanism of ice nucleation on model agi surfaces. *The Journal of Physical Chemistry B* 119, 9049–9055. URL: <http://dx.doi.org/10.1021/jp508601s>, doi:10.1021/jp508601s.